Laser-induced molecular alignment in dissociation dynamics

R. Numico, A. Keller, and O. Atabek
Laboratoire de Photophysique Moléculaire du CNRS, Bâtiment 213, Université Paris Sud, Campus d'Orsay, 91405 Orsay, France
(Received 2 March 1995)

Fragment angular distributions resulting from photodissociation induced by intense, short, linearly polarized laser pulses are investigated using a two-dimensional time-dependent split operator wave-packet propagation technique. The rotational excitation of the molecule leads, in general, to an alignment of the photofragments with respect to the field polarization vector but, unexpectedly, the reverse situation may also happen for some specific wavelengths for which fragmentation mainly occurs in a plane nearly orthogonal to the polarization axis. A detailed and comprehensive interpretation is provided referring to two typical wavelength regimes corresponding either to the blue or to the red wing of the single photon absorption line shape. The relevant strong field mechanisms upon which this interpretation rests are, respectively, the bond softening and the vibrational trapping of the molecule by the radiation which induces substantial modifications on the internal force field, viewed in the radiatively dressed adiabatic frame. An illustrative example, concerning the photodissociation of an isotropic distribution of ortho-H_2^+ in the $^2\Sigma_g^+(J=1/2, N=1, v=0)$ initial state, pertaining to Hund's (b) case, reveals that, at $\lambda = 1600$ Å, an efficient alignment is obtained with femtosecond pulses delivering an intensity in the range 10^{13}–10^{14} W/cm^2, as a consequence of the bond softening mechanism. More suprising is the possibility of observing fragments in a near orthogonal direction to the laser polarization, predicted by the trapping mechanism and confirmed by quantum calculations at shorter wavelengths, such as $\lambda = 800$ Å.

PACS number(s): 33.80.Gj, 33.80.Wz, 34.50.Ez, 42.50.Hz

I. INTRODUCTION

Recent progress in laser technology and in understanding atomic behavior in large radiation fields has renewed interest in the strong laser-induced multiphoton dissociation dynamics of molecules [1]. Both atoms and molecules are expected to undergo considerable distortion when exposed to intense radiation, but, due to their additional degrees of freedom which enrich the problem, molecular processes are even more intriguing. Following the initial excitation, stimulated absorption and emission mechanisms taking place during the fragmentation lead to product distributions (both scalar and vectorial) carrying information on the cumulative history of the overall dynamics. Two basically nonlinear intense field mechanisms resulting from the interplay between the multiphoton excitation step and subsequent radiative processes have recently been reported on in terms of bond softening (BS) or hardening [2]. The chemical bond can be softened by the laser-induced lowering of some potential energy barriers leading to efficient and fast photodissociation of low-lying vibrational levels [3–6]. Conversely, for some specific frequencies and intensities, the lifetime of high-lying resonances may increase with, as a consequence, a molecular bond which is harder to break. The molecule, confined by the laser in a finite region of the phase space, is stabilized through a vibrational trapping (VT) mechanism [7–11]. These mechanisms have repeatedly been evoked when interpreting or controlling *scalar* observables, such as total dissociation rates or energy spectra of the fragments.

Vectorial observables, such as angular distributions of the fragments, provide a complementary approach for the detailed understanding of the laser-molecule interaction dynamics. The most popular conviction so far experimentally supported by different observations is that molecules subjected to an intense, linearly polarized laser radiation preferentially dissociate in the direction of the polarization axis [3,4,12]. This explains the extensive use, by some theoreticians, of one-dimensional models where the fragmentation dynamics for a diatomic molecule is merely described by a single degree of freedom, namely, the internuclear distance [7–10,13–15]. Systematic experimental studies of fragmentation of molecular hydrogen in intense laser fields show, however, that the laser field begins to exert a torque on the molecule, leading to alignment and dissociation [16–18]. In addition, it is also observed that, at least for some wavelengths, protons are emitted along the polarization axis in narrow distributions that become broader as intensity increases [16]. Such experiments motivate the development of models where rotational degrees of freedom are fully included in order to provide an interpretation of the intensity dependence of fragment angular distributions. Actually, significant rotational excitation may take place during short intense pulses, which, as already discussed in previous theoretical works, can deeply modify the bond softening or stabilization mechanisms even by cancelling their effects for some wavelengths [11,19,20]. Finally, it is also to be noticed that angular distributions in the photodissociation of HD^+ have recently been investigated to control a possible isotope separation scheme [21].

The H_2^+ molecular ion in intense laser fields has been, during the last decade, one of the most popular systems of interest, for both experimental and theoretical studies dealing with above-threshold dissociation, BS and VT mechanisms, high harmonic generation, and alignment [3–10,13–15]. Measurements including kinetic energy spectra and angular distributions of fragments, as well as theoretical models for molecular alignment, so far concern picosecond and subpicosecond laser pulses with a light intensity ranging from 10^{13} W/cm^2 to 10^{15} W/cm^2. Moreover, the wavelengths in consideration are the Nd:YAG (where YAG denotes yttrium aluminum garnet) fundamental at 1.064 μm and its harmonics at 532 nm, 355 nm, 213 nm [11,16] or the Ti:sapphire fundamental at 780 nm and its harmonic at 390 nm [20] or some others such as 769 nm or 330 nm [13–15,19]. We wish to emphasize that all these wavelengths lead, in a dressed-state representation of matter-field interaction [22], to single photon avoided crossings occurring on the right of the ground state minimum (i.e., at larger internuclear distances than the equilibrium position): a situation analogous to a c^+ type of predissociation. As has been pointed out by Zavriyev *et al.* [16], for low-lying levels subject to c^+-type photodissociation, it is the BS mechanism which is the basis for an interpretive scheme of the alignment process. The other basic mechanism, namely, molecular stabilization, is attributed to higher vibrational levels trapped in laser-induced adiabatic potential wells. Such wells may, however, confine even very low-lying vibrational levels when they result from an avoided crossing occurring on the left of the ground state minimum (i.e., at shorter internuclear distances than the equilibrium position), that is, for wavelengths less than 115 nm leading to a c^- type of dissociation. Our aim, in this work, is to investigate fragment angular distributions in a systematic way by both varying the laser intensity and wavelength to cover c^+ -and c^--type dissociation processes and providing a theoretical background of molecular alignment phenomena in relation with the BS and VT mechanisms. Although intense laser pulses leading to c^--type curve crossing for H_2^+ ($\lambda < 115$ nm) are not yet available, the somewhat unexpected conclusions (the laser destroying the alignment), presenting a general range of validity, can be checked on other systems.

The paper is organized as follows. Section II provides the theoretical background for a time-dependent quantum model where a properly defined initial state of the H_2^+ ion is propagated on the lowest two Born-Oppenheimer potential curves radiatively coupled, in the so-called length gauge, by a classical laser pulse. The linearly polarized laser imposes a privileged direction in the laboratory frame (the polarization vector) with respect to which the molecular axis is positioned. The wave-packet propagation formalism involves two degrees of freedom, namely, the vibrational-translational motion R interacting, through the field, with the rotation θ around the polarization direction. The interaction itself, $\vec{\mu}\cdot\vec{\mathcal{E}}$ (the transition dipole moment $\vec{\mu}$ times the electric field $\vec{\mathcal{E}}$), depends upon θ. The computational technique implements a grid approach for the angle, following a recent scheme developed by Dateo and Metiu [23], and uses a unitary short-time propagator combined with split operator method and fast Fourier transforms. Fragment angular distributions are obtained by time integration of the instantaneous asymptotic current density flux. Section III presents angle-resolved dissociation probabilities for two wavelengths close to the maximum of the single photon absorption line shape of H_2^+ [for the transition $^2\Sigma_g^+(J=1/2,N=1,v=0)\rightarrow{}^2\Sigma_u^+$] for different intensities and pulse durations. The dynamics of alignment and the rotational energy transfer mechanism are thoroughly discussed in terms of BS and VT, which result from the specific laser wavelengths under consideration. Section IV is devoted to a brief summary and possible extensions.

II. THEORY

Our purpose is to examine the effect of rotational excitation on the time-dependent multiphoton dissociation of H_2^+ through the detailed understanding of fragment angular distributions at different laser wavelengths and intensities. Molecular hydrogen ion presents the advantage of a simple and known structure, involving within the Born-Oppenheimer approximation two electronic states well separated from the higher excited electronic manifold. The ground and dissociative states which describe the dissociation process,

$$H_2^+(1s\sigma_g)+n\hbar\omega\rightarrow H_2^+(2p\sigma_u)\rightarrow H^+ + H(1s), \qquad (1)$$

correspond to $(1s\sigma_g)^2\Sigma_g^+$ and $(2p\sigma_u)^2\Sigma_u^+$ symmetries, respectively. The potential energy curves, as well as the electronic transition moment $\mu=\langle 1s\sigma_g \mid r \mid 2p\sigma_u\rangle$, are taken from Bunkin and Tugov's fit [24]. The potential curves are displayed in Fig. 1 together with the two excitation wavelengths ($\lambda = 800$ Å and 1600 Å).

A. Basic features

The determination of the initial state, which is further used in a time-dependent wave-packet propagation, de-

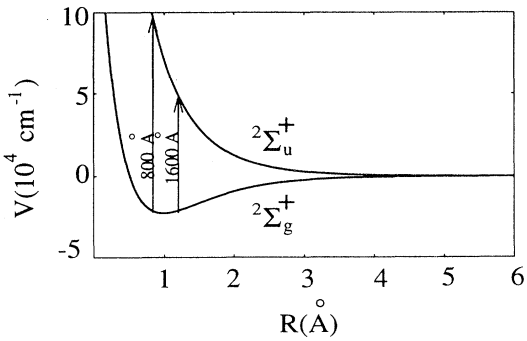

FIG. 1. H_2^+ ground ($^2\Sigma_g^+$) and first excited ($^2\Sigma_u^+$) Born-Oppenheimer states potential energy curves (in cm^{-1}) as a function of the internuclear distance (in Å). The vertical arrows indicate laser excitation frequencies corresponding to $\lambda = 1600$ Å and $\lambda = 800$ Å wavelengths.

serves particular interest. Basically, two characteristics of $H_2^+(^2\Sigma_g^+)$ have to be outlined: (i) the absence of spin-orbit coupling for Σ states ($\Lambda = 0$); and (ii) the antisymmetrical behavior of the total wave function for identical nuclei, which are fermions of half-integer spin. The first implies Hund's (b) case [25], where the relevant angular momentum vectors are indicated in Fig. 2 with respect to the laser polarization direction $\vec{\mathcal{E}}$. In traditional notations $\hat{L}$ indicates electron total orbital momentum (exclusive of electron spin) and $\hat{K}$ nuclear rotation angular momentum (exclusive of nuclear spin). For a $\Sigma(\Lambda = 0)$ state, $\hat{L}$ is perpendicular to the internuclear axis $\vec{R}$, as is $\hat{K}$. The total electron and nuclear rotation angular momentum (exclusive of nuclear and electron spin) $\hat{N} = \hat{L} + \hat{K}$ is also orthogonal to $\vec{R}$. The electronic spin $\hat{S}$ is decoupled from the molecular axis and has a quantum number $S = 1/2$ for $^2\Sigma$; but its projection on $\hat{R}$ is not defined. The total angular momentum (exclusive of nuclear spin) $\hat{J}$ is obtained by coupling $\hat{N}$ and $\hat{S}$, namely,

$$\hat{J} = \hat{N} + \hat{S} \tag{2}$$

so that the possible values of the quantum number J are $| N - S |, | N - S | + 1, \ldots, N + S$; that is,

$$J = N \pm 1/2. \tag{3}$$

We note that $\hat{J}$, $\hat{J}_{\vec{\mathcal{E}}}$ (the projection of $\hat{J}$ on the polarization axis with the corresponding quantum number M_J), $\hat{N}$, and $\hat{S}$ are conserved, whereas Ω, the projection of $\hat{J}$ on molecular axis $\vec{R}$, is not a good quantum number. Finally the initial $^2\Sigma_g^+$ state is an eigenfunction of $\hat{J}$, $\hat{J}_{\vec{\mathcal{E}}}$, $\hat{N}$, $\hat{S}$ and can, within good approximation, be taken as the eigenstate of a zeroth order Hamiltonian which neglects Coriolis interactions of $\hat{N} \cdot \hat{L}$ type:

$$H_0 = H_{el} + T_R + H_{rot}, \tag{4a}$$

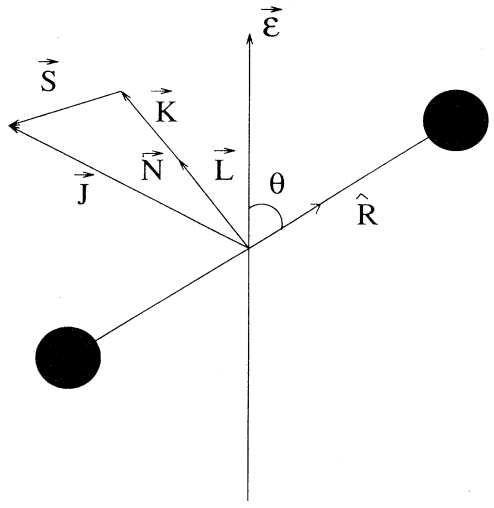

FIG. 2. Angular momentum vectors for $H_2^+(^2\Sigma_g^+)$ with respect to the polarization direction.

where

$$H_{el} = -\frac{\hbar^2}{2m_e}\frac{d^2}{dr^2} + U(r,R) + \frac{\hat{L}^2}{2m_e r^2}, \tag{4b}$$

$$T_R = -\frac{\hbar^2}{2m}\frac{d^2}{dR^2}, \tag{4c}$$

$$H_{rot} = \frac{\hat{N}^2}{2mR^2}, \tag{4d}$$

U being the potential energy, and m_e and m being the electron and reduced mass, respectively. In the Born-Oppenheimer frame the wave function is written as

$$\begin{aligned}\Psi_{^2\Sigma_g^+} &= r^{-1}R^{-1}\tilde{\Psi}_{^2\Sigma_g^+}(\vec{r},\vec{R}) \\ &= r^{-1}R^{-1}\phi_{el}(r)\Phi_{vN}(R) \\ &\langle \hat{r}, \hat{R} \mid \Lambda = 0, S = 1/2, J, M_J, N\rangle,\end{aligned} \tag{5}$$

where ϕ_{el} and Φ_{vN} are the spatial parts of the electronic orbital and of the nuclear vibrational motions, respectively, $\vec{r}$ and $\vec{R}$ being the corresponding electronic and nuclear coordinates. The angular part is expanded by using appropriate Clebsch-Gordan coefficients [26]:

$$\begin{aligned}| N, \Lambda, S, J, M_J\rangle = \sum_{M_N, M_S} & C(J, M_J \mid N, M_N; S, M_S) \\ & \times | N, \Lambda, M_N\rangle \mid S, M_S\rangle.\end{aligned} \tag{6}$$

The second point related with the homonuclear diatomic character of the molecule can be worked out by referring to the total wave function:

$$\Psi_{tot} = \Psi_{^2\Sigma_g^+}(\vec{r},\vec{R})\chi_N(1,2), \tag{7}$$

where χ_N is the nuclear spin function. Ψ_{tot} must be antisymmetric with respect to the interchange $1 \leftrightarrow 2$ of identical nuclei when these are fermions of half-integer spin as in H_2^+ (the spin of the proton is $I = 1/2$). We recall that the total nuclear spin number T is either 0 corresponding to a singlet function χ_N which is antisymmetrical, or 1 representing a symmetric triplet function χ_N [27]. For a ground state of $^2\Sigma_g^+$ symmetry, T=0 and 1 states are associated with rotational levels of even parity i.e., $N = 0, 2, 4, \ldots$ or odd parity, i.e., $N = 1, 3, 5, \ldots$, respectively, to ensure the overall antisymmetric character of Ψ_{tot}. Because of very small perturbations involving nuclear spins, singlet(T=0)-triplet(T=1) transitions are very rare events, such that molecular hydrogen rather consists of two distinct species: parahydrogen for which T=0 and orthohydrogen for which T=1, and in statistical equilibrium, at room temperature, the occurrence of ortho states is three times more probable than the para ones.

As a consequence of this analysis, the good quantum numbers for the $^2\Sigma_g^+$ ground state of ortho-H_2^+, in Hund's (b) case, take the following values: $\Lambda = 0$, $S = 1/2$, $J = 1/2$, $M_J = \pm 1/2$, $N = 1$, such that Eq. (6) leads to

$$| \Lambda = 0, S = 1/2; J = 1/2, M_J = \pm 1/2, N = 1\rangle$$

$$= \pm\frac{1}{\sqrt{3}} | N = 1, \Lambda = 0, M_N = 0\rangle | S = 1/2, M_S = \pm 1/2\rangle \pm \sqrt{\frac{2}{3}} | N = 1, \Lambda = 0, M_N = \pm 1\rangle | S = 1/2, M_S = \mp 1/2\rangle. \tag{8}$$

In this equation, the Wigner functions

$$\langle \theta, \phi | N, \Lambda, M_N\rangle = D^N_{M_N\Lambda}(\phi, \theta, 0) \tag{9}$$

for $\Lambda = 0$ are nothing but the spherical harmonics $Y_{N,M_N}(\theta, \phi)$ or associated Legendre polynomials $P_N^{M_N}(\cos\theta)$ given by [28]

$$D^N_{M_N\Lambda=0}(\phi, \theta, 0) = \sqrt{\frac{4\pi}{2N+1}} Y^*_{N,M_N}(\theta, \phi)$$
$$= (-1)^{M_N}\sqrt{\frac{(N+M_N)!}{(N-M_N)!}} e^{-iM_N\phi} \times P_N^{-M_N}(\cos\theta). \tag{10}$$

The spin-free Hamiltonian cannot mix states with different M_S, thus Eq. (8) appears as an incoherent sum of $M_N = 0, \pm 1$. We emphasize that to obtain results corresponding to an initial isotropic ensemble of molecules, in terms of sum of probabilities with $M_J = 1/2$ and $-1/2$, two calculations have to be performed based on Y_{10} and Y_{11} (Y_{1-1} leading to the same results as Y_{11} due to the fact that the total Hamiltonian does not depend upon the sign of M_N), and further combined using Eq. (8).

B. The two-dimensional short-time propagator

The time-dependent Schrödinger equation, in the Born-Oppenheimer frame, is written using 2×2 matrix notations as

$$i\hbar\hat{\mathbf{1}}\frac{d}{dt}\begin{pmatrix}\tilde{\Psi}_g\\ \tilde{\Psi}_u\end{pmatrix} = \hat{\mathbf{H}}\begin{pmatrix}\tilde{\Psi}_g\\ \tilde{\Psi}_u\end{pmatrix}, \tag{11}$$

where $\hat{\mathbf{H}}$ is the time-dependent total molecule-plus-field Hamiltonian given by

$$\hat{\mathbf{H}} = \hat{\mathbf{1}}(T_R + T_\theta + T_\phi) + \tilde{\mathbf{W}}(R, \theta; t), \tag{12}$$

$\hat{\mathbf{1}}$ being the identity matrix, and g and u the electronic labels of the ground and first excited states. The potential part includes the radiative coupling $\vec{\mu}\cdot\vec{\mathcal{E}}$. For a $\Sigma \to \Sigma$ transition, the dipole moment is parallel to the molecular axis $\hat{R}$, leading to [29]

$$\vec{\mu}\cdot\vec{\mathcal{E}} = -\mu(R)\cos\theta\epsilon(t)\cos\omega t, \tag{13}$$

where ω is the carrier wave frequency, and the laser pulse has a Gaussian shape:

$$\epsilon(t) = \epsilon_0 e^{-(t/\tau)^2}, \tag{14}$$

with τ as the half-width. Finally, $\tilde{\mathbf{W}}$ is written as

$$\tilde{\mathbf{W}} = \begin{pmatrix} V_g(R) & -\mu(R)\cos\theta\epsilon(t)\cos\omega t \\ -\mu(R)\cos\theta\epsilon(t)\cos\omega t & V_u(R)\end{pmatrix}, \tag{15}$$

where V's are the corresponding field-free molecular potential energies. Kinetic terms are given by Eq. (4c) for T_R, and by

$$T_\theta = -\frac{\hbar^2}{2mR^2}\frac{1}{\sin\theta}\frac{d}{d\theta}\left(\sin\theta\frac{d}{d\theta}\right), \tag{16}$$

$$T_\phi = -\frac{\hbar^2}{2mR^2}\frac{1}{\sin^2\theta}\frac{d^2}{d\phi^2}. \tag{17}$$

The initial wave packet, prior to the switching on of the field, is

$$\tilde{\mathbf{\Psi}}(t=0) = \begin{pmatrix}\chi_{gNv=0}(R)P_N^{M_N}(\cos\theta)e^{iM_N\phi}\\ 0\end{pmatrix}, \tag{18}$$

where $\chi_{gNv=0}$ is a solution of the radial Schrödinger equation:

$$\left[-\frac{\hbar^2}{2m}\frac{d^2}{dR^2} + V_g(R) - \frac{\hbar^2}{2mR^2}N(N+1) - E_{Nv=0}\right] \times\chi_{gNv=0}(R) = 0. \tag{19}$$

The motion associated with the azimuthal angle ϕ remains separated under the action of the ϕ-independent $\tilde{\mathbf{W}}$, as defined by Eq. (15), and M_N is a good quantum number describing the invariance through rotation about the field polarization vector. After factorization of this azimuthal part, the time-dependent total wave packet can be given the following compact form:

$$\tilde{\mathbf{\Psi}}_{M_N}(R, \theta, \phi; t) = e^{iM_N\phi}\mathbf{\Phi}_{M_N}(R, \theta; t), \tag{20}$$

where $\mathbf{\Phi}_{M_N}$ is to be calculated by solving the time-dependent Schrödinger equation:

$$i\hbar\frac{d}{dt}\mathbf{\Phi}_{M_N}(R, \theta; t) = [\mathbf{T}_R + \mathbf{T}_\theta + \mathbf{W}(R, \theta; t)]\,\mathbf{\Phi}_{M_N}(R, \theta; t), \tag{21}$$

with an effective potential term

$$\mathbf{W}_{M_N}(R,\theta;t) = \tilde{\mathbf{W}}(R,\theta;t) + \frac{\hbar^2}{2mR^2}\hat{\mathbf{1}}\frac{M_N^2}{\sin^2\theta}. \quad (22)$$

One of the most popular approaches for solving Eq. (21) is the use of Fourier transform methodology [30–33]. Problems involving angular variables have, however, most commonly been treated by a square integrable discrete basis set expansion in spherical harmonics combined with a Fourier grid for the radial motion [34,35]. The penalty turns out to be a prohibitive computational task when the number of spherical harmonics needed in the expansion is large. Recently, a new numerical Fourier transform method has been developed by Dateo and Metiu, based on a grid approach for the angle, implemented into a unitary Cayley scheme combined with a Feit-Fleck split operator technique [23]. The major advantage is, of course, the absence of matrix element evaluations and matrix multiplications other than fast Fourier transforms. The basic features of the method [23] which is based on the repeated use of the short-time propagator $U(\delta t)$:

$$\begin{aligned}\mathbf{\Phi}_{M_N}(R,\theta;t+\delta t) &= \mathbf{U}(\delta t)\mathbf{\Phi}_{M_N}(R,\theta;t)\\ &= \exp\left[-\frac{i}{\hbar}[\mathbf{T}_R + \mathbf{T}_\theta + \mathbf{W}_{M_N}(t)]\,\delta t\right]\\ &\quad\times\mathbf{\Phi}_{M_N}(R,\theta;t), \end{aligned} \quad (23)$$

involving the value of the effective potential term at time t, are outlined in the following. Since the three operators $\mathbf{T}_R$, $\mathbf{T}_\theta$, and $\mathbf{W}_{M_N}$ do not commute, the Moyal formula is applied twice, to obtain [36]

$$\begin{aligned}\exp\left[-\frac{i}{\hbar}[\mathbf{T}_R + \mathbf{T}_\theta + \mathbf{W}_{M_N}(t)]\,\delta t\right] &= \exp[-(i/\hbar)\mathbf{W}_{M_N}\delta t/2]\exp[-(i/\hbar)\mathbf{T}_\theta\delta t/2]\\ &\quad\times\exp[-(i/\hbar)\mathbf{T}_R\delta t]\exp[-(i/\hbar)\mathbf{T}_\theta\delta t/2]\\ &\quad\times\exp[-(i/\hbar)\mathbf{W}_{M_N}\delta t/2] + O(\delta t^3). \end{aligned} \quad (24)$$

All propagators appearing on the right-hand side of Eq. (24) are treated using the Feit-Fleck technique [30–33], except the one involving $\mathbf{T}_\theta$ approximated by Cayley's formula [37,23]

$$\begin{aligned}\exp[-(i/\hbar)\mathbf{T}_\theta\delta t/2] &= [1+(i/\hbar)\mathbf{T}_\theta\delta t/4]^{-1}\\ &\quad\times[1-(i/\hbar)\mathbf{T}_\theta\delta t/4]\\ &\quad+O(\delta t^3), \end{aligned} \quad (25)$$

which maintains unitarity ($\mathbf{T}_\theta$ being self-adjoint) and is further implemented in a way that avoids matrix inversion.

The action of potential and kinetic operators on the wave function $\mathbf{\Phi}_{M_N}(R,\theta;t)$ is evaluated by referring to a combination of coordinate and momentum representations, as is usual in this context. The Fourier transform theory associates with the grid points (R_p,θ_q) of the coordinate representation a wave vector grid (k_α,κ_β), and in what follows the values of the wave function at the grid points are labeled by the corresponding indices p, q, α, and β, i.e.,

$$\mathbf{\Phi}_{p,q}(t) = \mathbf{\Phi}_{M_N}(R_p,\theta_q;t). \quad (26)$$

The wave functions $\mathbf{\Phi}_{p,\beta}(t)$,$\mathbf{\Phi}_{\alpha,q}(t)$ in a mixed momentum-coordinate representation are related to $\mathbf{\Phi}_{p,q}(t)$, by a cosine transform for θ:

$$\mathbf{\Phi}_{p,q}(t) = \sum_{\beta=0}^{N_\theta}\zeta_\beta\cos(\kappa_\beta\theta_q)\mathbf{\Phi}_{p,\beta}(t) \quad (27a)$$

and a Fourier transform for R:

$$\mathbf{\Phi}_{p,q}(t) = \sum_{\alpha=-N_R/2}^{N_R/2-1}\exp(-ik_\alpha R_p)\mathbf{\Phi}_{\alpha,q}(t), \quad (27b)$$

where N_θ and N_R are the number of grid points, $\zeta_\beta = 1/2$ for $\beta = 0$ or N_θ while $\zeta_\beta = 1$ otherwise. All details concerning the relations between the grids in the two representations, as well as the inverse transforms of Eqs. (27), are indicated in Ref. [23]. The application of the short-time propagator $\mathbf{U}(\delta t)$ on the wave function $\mathbf{\Phi}(t)$ is schematically illustrated in Fig. 3. The different steps corresponding to Eqs. (24) and (25) are organized as follows from the upper to the lower part of the diagram.

(i) Circles W represent the action of the potential term which is local in the coordinate representation and results in

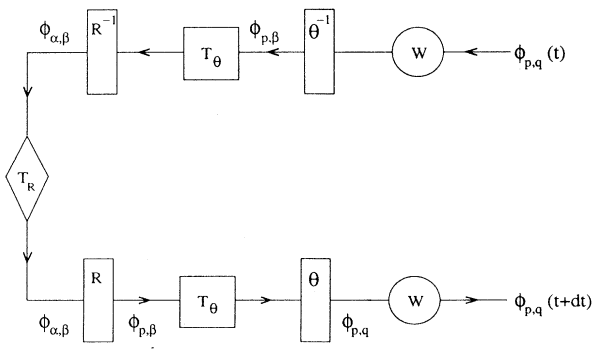

FIG. 3. Schematic representation for the evaluation of $\mathbf{U}(\delta t)\mathbf{\Phi}$ (see main text).

$$\exp\left[-(i/\hbar)\mathbf{W}_{M_N}(R_p,\theta_q;t)\delta t/2\right]\mathbf{\Phi}_{p,q}(t).$$

(ii) The angular kinetic energy is not diagonal in the plane wave representation. An original procedure based on a recurrence relation for $\mathbf{\Phi}_{p,\beta}(t+\delta t)$ in terms of its values $\mathbf{\Phi}_{p,\beta}(t)$ at an earlier time, in roughly N_θ operations, is given in Ref. [23], and can be recast in the following compact form:

$$\zeta_{\beta+1}a^*_{p,\beta+1}\mathbf{\Phi}_{p,\beta+1}(t+\delta t)-\zeta_{\beta-1}a^*_{p,\beta}\mathbf{\Phi}_{p,\beta-1}(t+\delta t)$$

$$-\zeta_{\beta+1}a_{p,\beta+1}\mathbf{\Phi}_{p,\beta+1}(t)+\zeta_{\beta-1}a_{p,\beta}\mathbf{\Phi}_{p,\beta-1}(t)=0 \quad (28)$$

(the asterisk indicates the complex conjugate), where

$$a_{p,\beta}=\left(\frac{2m}{\hbar}\right)R_p^2+i\frac{\delta t}{4}\kappa_\beta\kappa_{\beta-1} \quad (29)$$

for $\beta=1,\ldots,N_\theta-1$ and where

$$\mathbf{\Phi}_{p,N_\theta}(t+\delta t)=\mathbf{\Phi}_{p,N_\theta-1}(t+\delta t)=\mathbf{0} \quad (30)$$

is assumed. This is schematically indicated by the square boxes T_θ of Fig. 3 which are reached after an inverse cosine transform relating $\mathbf{\Phi}_{p,q}$ to $\mathbf{\Phi}_{p,\beta}$ [inverse transform of Eq. (27a)] symbolized by the vertical rectangle θ^{-1}.

(iii) The rhomb T_R represents the action of the radial kinetic energy which is diagonal in a momentum representation $\mathbf{\Phi}_{\alpha,\beta}$ obtained by Fourier transforming $\mathbf{\Phi}_{p,\beta}$; an operation symbolized by the vertical rectangle R^{-1} [inverse transform of Eq. (27b)]. The result after the T_R rhomb is merely:

$$\exp\left[-(i\hbar k_\alpha^2/2m)\delta t\right]\mathbf{\Phi}_{\alpha,\beta}(t).$$

The lower part of the diagram is straightforward: $\mathbf{\Phi}_{p,q}(t+\delta t)$ in the coordinate representation results by applying the indicated Fourier transforms together with kinetic and potential operators building up Eq. (24).

C. Fragment angular distribution

The observable to be ultimately reached is the fragment angular distribution defined as the probability to asymptotically (i.e., at $t\to\infty$ and at large nuclear separation $R\geq R_0$) obtain a photofragment in a conical volume delimited by the solid angle:

$$d\Omega=\sin\theta d\theta d\phi \quad (31)$$

as indicated in Fig. 4. In terms of the Ψ_g and Ψ_u components of the wave packet, defined in Eq. (11), this angular resolved probability can be written as the triple integral

$$\mathcal{P}(\theta,\phi)=\lim_{t\to\infty}\int_{\theta-d\theta/2}^{\theta+d\theta/2}d\theta'\sin\theta'\int_{\phi-d\phi/2}^{\phi+d\phi/2}d\phi'\int_{R_0}^{\infty}dR\,R^2\left[|\Psi_g(R,\theta,\phi;t)|^2+|\Psi_u(R,\theta,\phi;t)|^2\right] \quad (32)$$

on the conical volume element $R^2d\Omega$. R_0 is chosen far enough that the bound state components of the asymptotic wave packet can be safely neglected. It has to be noticed that a prerequisite of the calculation involved in Eq. (32) is the accurate knowledge of the asymptotic wave-packet components Ψ_g and Ψ_u at time $t\to\infty$. This constitutes, in general, a real challenge, not only because of the long propagation time it necessitates, but basically because of the spreading of the wave packet on large spatial grids. To overcome this difficulty various methods have been suggested, the most efficient one seeming to be the use of current density combined with absorbing boundary conditions (so-called optical potentials) [38]. Similarly, one can refer to the radial behavior of the asymptotic flux. More precisely, the current density (or flux) vector $\vec{\mathcal{J}}$ being defined as

$$\vec{\mathcal{J}}=\vec{\mathcal{J}}_g+\vec{\mathcal{J}}_u, \quad (33a)$$

with

$$\vec{\mathcal{J}}_k=\frac{\hbar}{2mi}\left[\Psi_k^*\vec{\nabla}\Psi_k-\Psi_k\vec{\nabla}\Psi_k^*\right]\ (k=g,u), \quad (33b)$$

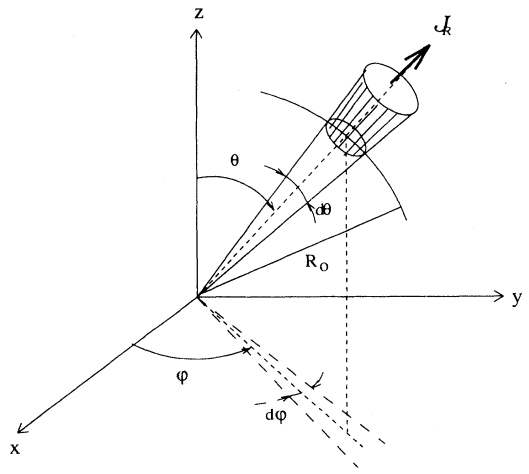

FIG. 4. Conical volume delimited by the solid angle $d\Omega=\sin\theta d\theta d\phi$ in the laboratory frame, through which the flux is calculated. The truncated asymptotic cone ($R\geq R_0$) is illustrated by the hatched surface $\mathcal{S}_c$ of volume $\mathcal{V}_c$ (see main text).

the time-dependent Schrödinger equation leads to

$$\frac{d}{dt}\left[|\Psi_g(R>R_0)|^2+|\Psi_u(R>R_0)|^2\right]=-\vec{\nabla}\cdot\mathcal{J}, \quad (34)$$

allowing the evaluation of $\mathcal{P}(\theta,\phi)$ in terms of two expressions related by Green's theorem, namely

$$\mathcal{P}(\theta,\phi)=\int dt\int\int\int_{\mathcal{V}_c}\left(-\vec{\nabla}\cdot\vec{\mathcal{J}}\right)dv$$
$$=\int dt\int\int_{\mathcal{S}_c}\vec{\mathcal{J}}\cdot d\vec{S}, \quad (35)$$

$\mathcal{V}_c$ and $\mathcal{S}_c$ being, respectively, the volume and the surface of the asymptotic truncated cone of Fig. 4. As was already mentioned, the important simplifying feature is that the total flux vector $\vec{\mathcal{J}}$ is radial outside the sphere of radius R_0 defining the asymptotic region of Eqs. (32) and (35). This can be shown by taking R_0 such that, for $R>R_0$, the R^{-2}-dependent rotational part of the Hamiltonian will be negligible as compared to the radial kinetic part (i.e., $\|T_\theta\| \ll \|T_R\|$). The resulting time-depent coupled equations can be written as

$$i\hbar\frac{d}{dt}\Psi_k=-\frac{\hbar^2}{2m}\frac{1}{R}\frac{d^2}{dR^2}R\Psi_k+V_k\Psi_k-\mu\epsilon\cos(\omega t)\cos(\theta)\Psi_{k'}$$

$$\text{with } k\neq k'=g,u \text{ and for } R>R_0. \quad (36)$$

After straightforward algebra involving multiplication of Eq. (36) by Ψ_k^* and subtracting its complex conjugate, the operation being summed up for $k=g$ and u, one gets

$$\frac{d}{dt}\left[|\Psi_g(R>R_0)|^2+|\Psi_u(R>R_0)|^2\right]=-\frac{1}{R^2}\frac{d}{dR}R^2\mathcal{J}_R, \quad (37)$$

where $\mathcal{J}_R$ is the radial part of $\vec{\mathcal{J}}$. The asymptotic wave packets $\Psi_k(R>R_0)$, solutions of Eq. (36) without rotational dynamics (calculated at fixed value of θ and ϕ) result, through Eq. (37), in a radial flux vector $\mathcal{J}_R(\theta,\phi;t)$ illustrated in Fig. 4. In other words, the flux reaching the cone $d\Omega$ at R_0 will remain in this cone at any further time and will ultimately lead to the fragment angular distribution

$$\tilde{\mathcal{P}}(\theta,\phi)=\frac{d\mathcal{P}(\theta,\phi)}{d\Omega}=\int dt\, R_0^2\mathcal{J}_R(R_0,\theta;t). \quad (38)$$

Practically, this means that wave packets have to be propagated until they reach $R=R_0$, where a time-dependent flux $\mathcal{J}_R(R_0,\theta;t)$ is calculated using Eq. (33b), the final distribution being obtained from Eq. (38). The necessity of large distance propagation due to important spreading of the wave packet being avoided, this technique is much more efficient and tractable than the one involved in Eq. (32). It is worthwhile noting that this analysis is conducted by referring to a given M_N, although for convenience, the index M_N of $\tilde{\mathcal{P}}_{M_N}(\theta,\phi)$ has been dropped so far [cf. Eq. (38)]. Fragment angular distributions for an isotropic initial ensemble of molecules are obtained, using Eq. (8), from the following incoherent sum:

$$\tilde{\mathcal{P}}_{tot}(\theta,\phi)=\sum_{M_J=\pm1/2;M_N=0,\pm1}C^2(J,M_J\mid N,M_N;S,M_S)$$
$$\times\tilde{\mathcal{P}}_{M_N}(\theta,\phi), \quad (39)$$

which results in

$$\tilde{\mathcal{P}}_{tot}(\theta,\phi)=1/3\tilde{\mathcal{P}}_0(\theta,\phi)+2/3\tilde{\mathcal{P}}_1(\theta,\phi). \quad (40)$$

Finally the cylindrical symmetry with respect to the z axis (laser polarization direction) manifests itself by ϕ invariance of the radial flux, such that integration over ϕ of Eq. (38) merely provides a 2π factor. The normalized total θ-dependent dissociation probability is ultimately given by

$$\mathcal{P}_{norm}(\theta)=\frac{\tilde{\mathcal{P}}_{tot}(\theta)}{\int_0^\pi d\theta\sin\theta\tilde{\mathcal{P}}_{tot}(\theta)}, \quad (41)$$

where

$$\tilde{\mathcal{P}}_{tot}(\theta)=\int_0^{2\pi}d\phi\,\tilde{\mathcal{P}}_{tot}(\theta,\phi)=2\pi\int_0^\infty dt R_0^2\mathcal{J}_R(R_0,\theta;t). \quad (42)$$

III. RESULTS

Starting from the $H_2^+(^2\Sigma_g^+, v=0, J=1/2, N=1)$ state [Eq. (8)], and using a linearly polarized, short, intense laser pulse we study fragment angular distributions for two different wavelength regimes, as indicated in Fig. 1. The wavelength dependence of possible alignment processes is the basic concern of this section. Field intensity, pulse shape, and duration effects are also analyzed within a comprehensive interpretation frame.

A. Wavelength dependence of angular distributions

The full two-dimensional calculations which are presented have been carried out with a Gaussian pulse [Eq. (14) with $\tau\sim10$ fs duration] of intensity ranging from 10^{13} up to 10^{14} W/cm^2. Normalized dissociation probabilities as a function of the detection angle θ with respect to the laser polarization vector are gathered in Figs. 5(a) and 5(b). The upper panel (a) corresponds to a wavelength $\lambda=1600$ Å (taken in the red wing of the absorption line shape) and shows an intensity-dependent alignment. As has already been discussed in the literature [16,20], increasing alignment with stronger laser intensity as compared to the angular distribution with the $\frac{3}{2}\cos^2\theta$ shape [39] expected in the weak field regime for a single-photon Σ-Σ direct photodissociation is observed. A much more surprising result is the one displayed in the lower panel (b) corresponding to an excitation with a wavelength $\lambda=800$ Å (taken in the blue wing of the absorption line shape) where, unexpectedly, the reverse situation holds: fragments are less and less aligned with increasing laser intensity. Normalized dissociation prob-

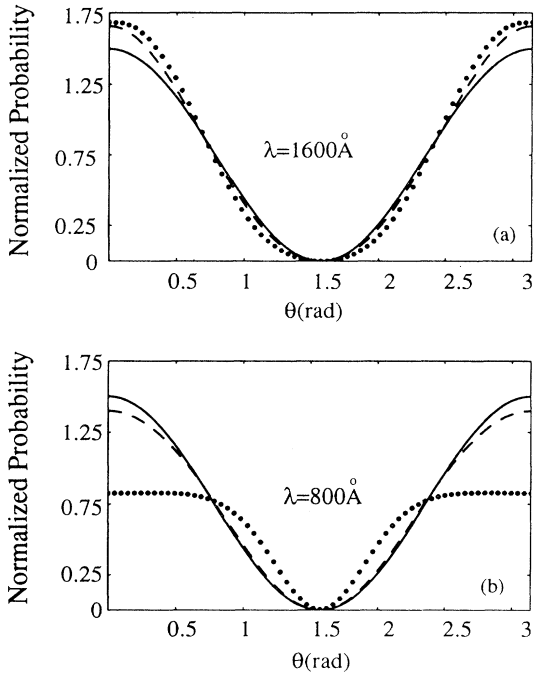

FIG. 5. Normalized dissociation probabilities $\mathcal{P}_{norm}(\theta)$ as a function of the detection angle θ(rad) with respect to the field polarization direction. The Gaussian pulse duration is $\tau = 10$ fs [cf. Eq. (14) of main text]. The solid line corresponds to the weak field $\frac{3}{2}\cos^2\theta$ shape. The dashed and dotted lines are for $I = 10^{13}$ W/cm^2 and $I = 10^{14}$ W/cm^2, respectively. Panel (a) is for $\lambda = 1600$ Å and panel (b) for $\lambda = 800$ Å.

abilities $\mathcal{P}_{norm}(\theta)$, around $\theta = 0$ and π, are decreasing with respect to their standard weak field values given by $\frac{3}{2}\cos^2\theta$ (i.e., 1.5). Our aim, besides showing such wavelength-dependent unexpected behaviors, is to analyze how the dissociation dynamics proceeds and how angular momentum is transferred from the electromagnetic field to the molecule by referring to some nonlinear intense radiative interaction mechanisms.

B. One-dimensional fixed-angle models

We claim that at least some of the basic features of the alignment process can be understood in terms of fixed-angle one-dimensional models. These models, where the rotational motions are frozen ($T_\theta = T_\phi = 0$), carry the angular information only through the radiative interaction term, which can simply be written as proportional to $\mu\cos\theta\sqrt{I}$, I being the laser peak intensity. In order for a Floquet picture to roughly hold, we take a quasi-continuous wave laser with rising and falling wings identical to that of the previous Gaussian pulse ($\tau = 10$ fs); i.e.,

$$\epsilon(t) = \begin{cases} \epsilon_0 e^{-(t-t_0)^2/\tau^2} & \text{for } t < t_0, \text{ with } t_0 = 35 \text{ fs} \\ \epsilon_0 & \text{for } t_0 < t < T, \text{ with } T = 65 \text{ fs} \\ \epsilon_0 e^{-(t-t_0-T)^2/\tau^2} & \text{for } t > T. \end{cases} \quad (43)$$

Within these assumptions, the single-photon dressed molecular states of H_2^+ are indicated in Fig. 6. In the diabatic frame, where the ground state potential $V_g(R)$ is merely shifted by the photon energy, the resulting curve crossing with the excited state potential $V_u(R)$ corresponds to one of the two possible configurations: either a c^+-type crossing (right of the equilibrium position) in the case of $\lambda = 1600$ Å radiation, or a c^--type crossing (left of the equilibrium position) in the case of $\lambda = 800$ Å radiation. These situations are depicted in panels (a) and (b) of Fig. 6. For intense fields, a more realistic molecule-plus-field view is the adiabatic frame obtained by diagonalizing the radiative coupling. Typical adiabatic potential energy curves (for $I = 10^{14}$ W/cm^2 and $\theta = 0$) are also indicated in Figs. 6(a) and 6(b).

Different dissociation mechanisms have to be invoked for the case of c^+- or c^--type crossings, in relation with the time-dependent behavior of the survival probability, given as the projection of the θ-fixed total wave packet on the vibrational states of the ground electronic state:

$$P_{survival}(t) = \sum_{v,k=g,u} |\langle \chi_{gv}(R) \mid \tilde{\Psi}_{k,M_n}(R, \theta = 0, \phi; t)\rangle|^2, \quad (44)$$

which is also indicated in Fig. 6(c), together with the pulse shape.

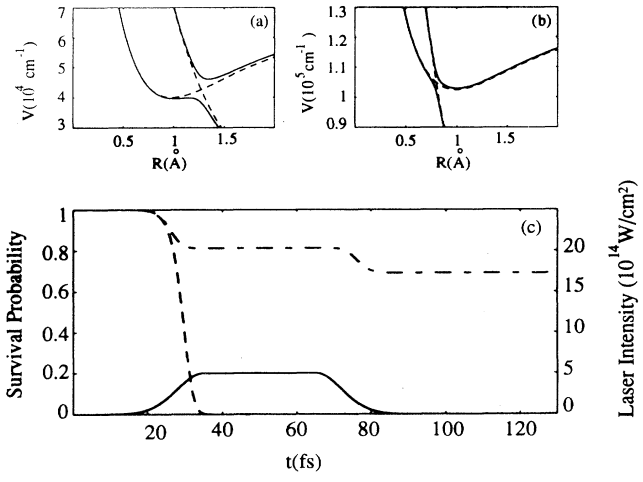

FIG. 6. Panels (a) and (b) represent diabatic (dashed line) and adiabatic (solid line) dressed potentials of H_2^+ with $\lambda = 1600$ Å and $\lambda = 800$ Å, respectively. Panel (c) shows the survival probability as a function of time in femtoseconds (for $\theta = 0$) when excited by the long duration laser pulse indicated by the solid line (intensity scale 10^4 W/cm^2 on the right). The dashed and dashed-dotted lines correspond to $\lambda = 1600$ Å and $\lambda = 800$ Å wavelengths, respectively.

1. c^+-type crossing ($\lambda = 1600$ Å)

This is the standard case describing multiphoton processes abundantly discussed in the literature as the manifestation of a new field effect called "bond softening." The adiabatic potential barrier [Fig. 6(a)] is lowered in an efficient way and proportional to the radiative coupling, i.e., $\sqrt{I}\cos\theta$. For a given intensity this lowering is much more important for $\cos\theta \sim 1$, that is, for $\theta \sim 0$ or π. For $\cos\theta \sim 0 (\theta \sim \pi/2)$ the high potential barrier is hardly penetrable. At first approximation, molecules roughly aligned with the field are the ones which efficiently dissociate (the survival probability decreases very fast to zero as the laser is switched on), leading to photofragments close to the direction $\theta = 0$ or π.

2. c^--type crossing ($\lambda = 800$ Å)

The high-field mechanism which is the leading one is the "vibrational trapping." The laser is confining the molecule in a short distance range internal region. 80% of the dissociation is temporarily stopped during the laser pulse and, as indicated in Fig. 6(c), the final survival probability remains 0.7. This process can be interpreted in terms of the wave packet trapped in the upper close adiabatic potential [Fig. 6(b)]. The increase of the radiative interaction (either for $\theta = 0, \pi$ or for stronger fields) results in even more efficient trapping, due to the fact that the remaining kinetic (nonadiabatic) couplings of the adiabatic frame are decreasing accordingly. More precisely, the nonadiabatic kinetic couplings, responsible for the dissociation in this case, are sharply peaked around the avoided crossing position with a strength roughly three times larger for $\theta \sim \pi/2$ (no coupling at $\theta = \pi/2$) than for $\theta = 0$ or π. The dissociation process is slowed down for $\theta = 0$ and π in favor of an increase at angles close to $\theta \sim \pi/2$ (no dissociation occurring at $\theta = \pi/2$).

C. Predictive ability and limitations of fixed-angle models

The validity of an interpretive model, such as the one we are considering, can be checked and so can its predictive ability. For the critical c^- -type crossing, it is naturally expected that the previous trends be enhanced by increasing the pulse duration or intensity: the system being more efficiently confined during a longer time or in a larger region of space around $\theta = 0$ or π, its dissociation is lowered in these directions and the probability to observe fragments in a plane orthogonal to the laser polarization direction increases. The result of a full two-dimensional calculation with $\lambda = 800$ Å, $I = 10^{14}$ W/cm^2 and the long duration pulse of Eq. (43) is compared to the short pulse case in Fig. 7(a). This comparison (same intensity, but longer pulse) nicely illustrates the predictive ability of the fixed-angle model: not only does the alignment probability decrease, but the final angular distribution exhibits two clearly marked maxima around a hole at $\theta \sim \pi/2$ for which no dissociation is observed. For the same long duration pulse, the increase of the field intensity up to $I = 5 \times 10^{14}$ W/cm^2 leads to even more curious results. Actually, interesting observations can be done by analyzing the outcome of the two-dimensional calculations of Fig. 7(b): (i) the angular distribution is more peaked around the hole at $\theta \sim \pi/2$, the amplitude of the two maxima is enhanced, whereas the angular distance which separates them is less; (ii) a non-negligible percentage ($\sim 10\%$) of fragments is observed in a plane orthogonal to the polarization direction ($\theta = \pi/2$), although there is no radiative coupling at this precise direction; and (iii) a small increase of alignment probability (at $\theta = 0$ and π) results in the appearance of two wings in the angular distribution. If the first point is a natural consequence of the fixed-angle model, the two others cannot be explained in the same frame, appearing thus as limitations of the one-dimensional interpretation.

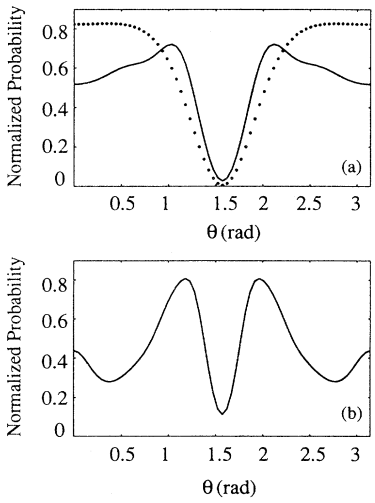

FIG. 7. Normalized dissociation probabilities $\mathcal{P}_{norm}(\theta)$ as a function of the angle θ (rad) with respect to the field polarization direction for an excitation wavelength $\lambda = 800$ Å. Panel (a) corresponds to an intensity $I = 10^{14}$ W/cm^2, dots for the short Gaussian pulse and solid line for the long duration pulse [cf. Eq. (43) of main text]. Panel (b) corresponds to $I = 5 \times 10^{14}$ W/cm^2 with a long duration pulse.

D. Rotational energy transfer mechanism

The fixed-angle model, through the analysis of dissociation dynamics on a molecule-plus-field surface (in R,θ space), indicates that molecules having a given initial alignment (i.e., parallel or near orthogonal to the polarization direction for c^+- or c^--type excitations, respectively) preferentially dissociate following these particular directions, leading to aligned or out of alignment photofragments. But obviously such a simple model cannot account for the rotational excitation occurring during the dissociation itself which is also responsible for alignment, as is clear from recent two-laser experiments on CO

[17] and I_2 [40]. Basically, two rotational energy transfer mechanisms have been evoked.

(i) Multiphoton interaction involving several absorption and stimulated emission processes results in an efficient "rotational pumping" to high angular momenta J [20]. However, for the wavelengths under consideration, a near resonance single-photon mechanism is the leading one, thus avoiding high J population. Incidentally, we note that this is the reason why the distributions presented in this work are not so sharply peaked.

(ii) A significant torque the laser field begins to exert on the molecule leads to some preferential alignments resulting in efficient dissociation [16].

It is precisely this last mechanism which is ignored in the fixed-angle model. Its effect can quantitatively be examined by comparing a full two-dimensional calculation with a succession of fixed-angle calculations for several discrete values of θ taken as a parameter [by neglecting the kinetic terms T_θ and T_ϕ of Eqs. (16) and (17)]. The results of these calculations, in terms of fragment angular distributions, are presented in Fig. 8, for the long duration pulse of Eq. (43) and a peak intensity of $I = 10^{14}$ W/cm^2. The c^+ and c^- cases deserve separate discussions.

1. c^+-type crossing [λ = 1600 Å, Fig. 8(a)]

Marked features distinguish the two approaches: the two-dimensional model not only leads to more aligned fragments but also results in more efficient total dissociation probability ($P_{tot} = 0.97$) than the fixed-angle model ($P_{tot} = 0.73$). A schematic understanding can be provided by referring to the local two-dimensional lower adiabatic molecule-plus-field potential energy surface (in the R, θ space) which monitors the dissociation dynamics. A three-dimensional (3D) viewgraph of this surface, in the vicinity of its barrier, is given in Fig. 9. Clearly, in the fixed-angle model and with a classical view in mind, only trajectories with appropriate initial conditions, namely, along $\theta = 0$ or π, can be considered to proceed to the outer, large distance part of the surface leading to the dissociative valley. Those starting with $\theta \sim \pi/2$ will be obstructed by the potential barrier which is hardly penetrable at these angles. The two-dimensional model adds a dynamical flexibility to the rotational motion. The torque which is exerted at short distances allows the trajectories to skirt around the potential barrier and find the minimum energy pathway towards the dissociative valley (that is, for directions close to $\theta = 0$ or π). The total dissociation probability is thus enhanced. In the later steps the large distance dynamics is no longer affected by an additional torque (due to the R^{-2} factor in T_θ) so that fragment angular distribution is close to its value at the position of the barrier, where alignment with the field ($\theta = 0$ or π) is favored. A closer inspection of Fig. 8(a) shows that the angular distribution is actually peaked at angles θ in the vicinity of 0 and π, but not accurately at these values. This is in relation to the long duration intense pulse which favors an efficient rotational energy transfer on the $M_N = \pm 1$ components.

2. c^--type crossing [λ = 800 Å, Fig. 8(b)]

Fragment angular distributions in the direction of the field (i.e., at $\theta = 0$ or π) are more favored in the fixed-angle model, but the two-dimensional model leads to some probability at $\theta = \pi/2$, whereas, as expected, no such fragments are observed in the fixed-angle model. Here the dissociation mechanism is initiated by a nonadiabatic jump from the attractive upper to the repulsive lower adiabatic surface. This is monitored by a nonadiabatic kinetic interstate coupling located at the avoided

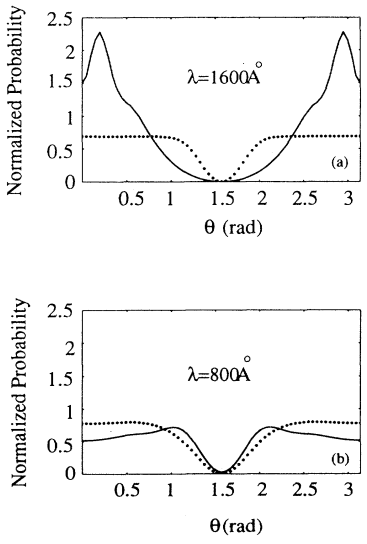

FIG. 8. Normalized dissociation probabilities $\mathcal{P}_{norm}(\theta)$ as a function of the detection angle θ (rad) with respect to the field polarization direction for an intensity of $I = 10^{14}$ W/cm^2 and the long duration pulse [cf. Eq. (43) of main text] with two excitation wavelengths $\lambda = 1600$ Å (a) and $\lambda = 800$ Å (b). The solid line corresponds to a full two-dimensional calculation and the dotted line to a fixed-angle model result.

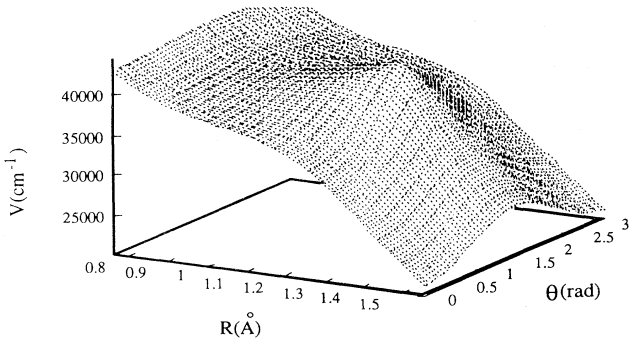

FIG. 9. 3D schematic view of the lower adiabatic molecule-plus-field surface in the vicinity of the potential barrier. R is in Å, θ in rad, and the energies are in cm^{-1}.

crossing point and presenting an amplitude maximum for $\theta \sim \pi/2$. As has previously been quoted, the kinetic coupling at $\theta = 0$ or π is three times less, but somewhat larger in extension over R. In the fixed-angle model and again within a classical view in mind, trajectories with an initial angle close to $\pi/2$ dissociate slightly more efficiently than those with angle $\theta = 0$ or π. But statistically, with an equal weighting for a homogeneous θ sampling, the dissociation probability although low is not very θ sensitive, as there is some surface jump probability even for $\theta = 0$ or π. But, of course, one observes a hole at $\theta = \pi/2$ where there is no radiative coupling at all. In the two-dimensional model, the molecule is affected by an important rotational momentum at short distances R, corresponding to the left avoided crossing. Rotational excitation to $\theta \sim \pi/2$, resulting in nonadiabatic jump followed by dissociation on the lower adiabatic surface, is the leading mechanism, as can be seen by a significant enhancement of fragment angular distribution at 1 and 2 rad. Finally the nonzero fragmentation probability at $\theta = \pi/2$ can be interpreted in terms of the torque which continues to act on the molecule during later dynamics on the lower surface.

IV. CONCLUSIONS

In this paper we present an outline for a comprehensive study of the angular distribution of photofragments resulting from the interaction of a molecular ion with a short, intense laser pulse. The interpretation relies basically on the interplay of field-induced chemical bond softening and hardening mechanisms. The rotational excitation process is analyzed in terms of the torque the linearly polarized laser exerts on the dissociating molecule. The widely discussed alignment of the molecular axis with respect to the polarization vector, leading to fragments along this direction, is related to the bond softening mechanism occurring in multiphoton excitation processes. But the most original finding is the possibility, at least for some wavelengths, to observe photofragments in a plane orthogonal to the polarization axis, a possibility enhanced by the high intensity and the long duration of the laser pulse. The detailed dynamical understanding of such data calls for an angle-dependent bond hardening model involving very efficient trapping in all spatial directions except a direction quasiperpendicular to the applied field where fragmentation may take place.

The H_2^+ ion, to which a large amount of experimental and theoretical research is currently devoted, is taken as an illustrative example, although the necessary adjustment between molecular force field (potential energy curves) and laser characteristics to obtain the desired trapping effect requires an intensity regime within a wavelength domain which is not yet achieved. This is why future theoretical work has to be oriented towards other systems by suggesting experiments aiming at the intense laser control of photofragment angular distributions by frequency tuning. Work is also under progress in our group to analyze in detail the dynamical behavior of H_2^+ submitted to radiative interaction with longer wavelengths for which experimental data are available [16] by accurately evaluating angle-resolved fragment kinetic energy distributions in the above-threshold dissociation domain.

ACKNOWLEDGMENTS

We acknowledge a grant of computing time on Cray C-98 from Institut du Developpement et des Ressources en Informatique Scientifique I.D.R.I.S. under Project No. 940425.

[1] *Coherence Phenomena in Atoms and Molecules in Laser Fields*, Vol. 287 of *NATO Advanced Study Institute, Series B: Physics*, edited by A. D. Bandrauk and S. C. Wallace (Plenum, New York, 1992).
[2] G. Yao and S. I. Chu, Chem. Phys. Lett. **197** 413 (1992); Phys. Rev. A **48**, 485 (1993).
[3] P. H. Bucksbaum, A. Zavriyev, H. G. Muller, and D. W. Schumacher, Phys. Rev. Lett. **64**, 1883 (1990).
[4] B. Yang, M. Saeed, L. F. Di Mauro, A. Zavriyev, and P. H. Bucksbaum, Phys. Rev. A **44**, R1458 (1991).
[5] A. D. Bandrauk, E. Constant, and J. M. Gauthier, J. Phys. II (France) **44**, 1033 (1991).
[6] G. Jolicard and O. Atabek, Phys. Rev. A **46**, 5845 (1992).
[7] A. D. Bandrauk and M. L. Sink, J. Chem. Phys. **74**, 1110 (1981).
[8] A. Giusti-Suzor and F. H. Mies, Phys. Rev. Lett. **68**, 3869 (1992).
[9] O. Atabek, M. Chrysos, and R. Lefebvre, Phys. Rev. A **49**, R8 (1994).
[10] O. Atabek, Int. J. Quantum Chem. Symp. **28**, 113 (1994).
[11] E. E. Aubanel, J. M. Gauthier, and A. D. Bandrauk, Phys. Rev. A **48**, 2145 (1993).
[12] K. Codling and L. J. Frasinski, J. Phys. B **26**, 783 (1993).
[13] A. Giusti-Suzor, X. He, O. Atabek, and F. H. Mies, Phys. Rev. Lett. **64**, 515 (1990).
[14] M. Chrysos, O. Atabek, and R. Lefebvre, Phys. Rev. A **48**, 3845 (1993); **48**, 2855 (1993).
[15] H. Abou-Rachid, T. T. Nguyen-Dang, R. K. Chaudhury, and X. He, J. Chem. Phys. **97**, 5497 (1992).
[16] A. Zavriyev, P. H. Bucksbaum, H. G. Muller, and D. W. Schumacher, Phys. Rev. A **42**, 5500 (1990).
[17] D. Normand, L. A. Lompré, and C. Cornaggia, J. Phys. B **25**, L497 (1992).
[18] D. T. Strickland, Y. Beaudoin, P. Dietrich, and P. B. Corkum, Phys. Rev. Lett. **68**, 2755 (1992).
[19] E. E. Aubanel, A. Conjusteau, and A. D. Bandrauk, Phys. Rev. A **48**, R4011 (1993).
[20] E. Charron, A. Giusti-Suzor, and F. H. Mies, Phys. Rev. A **49**, R641 (1994).
[21] E. Charron, A. Giusti-Suzor, and F. H. Mies, Phys. Rev.

Lett. **71**, 692 (1993).
[22] C. Cohen-Tannoudji and S. Reynaud, in *Multiphoton Processes,* edited by J. H. Eberly and P. Lambropoulos (Wiley, New York, 1983).
[23] C. E. Dateo and H. Metiu, J. Chem. Phys. **95**, 7392 (1991).
[24] F. V. Bunkin and I. I. Tugov, Phys. Rev. A **8**, 601 (1973).
[25] M. Mizushima, *The Theory of Rotating Diatomic Molecules* (John Wiley and Sons, New York, 1975), p. 132.
[26] A. R. Edmonds, *Angular Momentum in Quantum Mechanics* (Princeton University Press, Princeton, NJ, 1957).
[27] B. H. Bransden and C. J. Joachain, *Physics of Atoms and Molecules* (Longman Scientific and Technical, New York, 1988), pp. 453 and 454.
[28] D. A. Varshalovich, A. N. Moskalev, and V. K. Khersonskii, *Quantum Theory of Angular Momentum* (World Scientific, Singapore, 1988).
[29] H. Lefebvre Brion, *Perturbations in The Spectra of Atoms and Molecules* (Academic Press, New York, 1986).
[30] See, for instance, *Time-Dependent Methods for Quantum Mechanics*, edited by K. C. Kulander, special issue of Comput. Phys. Commun. **63** (1991).
[31] R. Kosloff, J. Phys. Chem. **92**, 2087 (1988).
[32] H. D. Feit, J. A. Fleck, and A. Steiger, J. Comput. Phys. **47**, 412 (1982).
[33] H. D. Feit and J. A. Fleck, Jr., J. Chem. Phys. **78**, 301 (1983); **80**, 2578 (1984).
[34] R. C. Mowrey and D. J. Kouri, J. Chem. Phys. **84**, 6466 (1986); **86**, 2087 (1987).
[35] R. Heather and H. Metiu, Chem. Phys. Lett. **157**, 505 (1989).
[36] J. E. Moyal, Proc. Cambridge Philos. Soc. **45**, 99 (1949).
[37] K. Yosida, *Functional Analysis* (Springer-Verlag, New York, 1971), p. 202.
[38] D. Neuhasuer and M. Baer, J. Chem. Phys. **90**, 4351 (1989), and references therein.
[39] R. N. Zare, *Angular Momentum* (John Wiley and Sons, New York, 1988), p. 119.
[40] P. Dietrich, D. T. Strickland, M. Laberge, and P. B. Corkum, Phys. Rev. A **47**, 2305 (1993).